

Effects of Lorentz invariance violation on particle and photon production in astrophysical sources

Matheus Duarte and Vitor de Souza

Instituto de Física de São Carlos, Universidade de São Paulo, Av. Trabalhador São-carlense 400, São Carlos, Brazil

E-mail: matheus_duarte@usp.br, vitor@ifsc.usp.br

Abstract. We investigate the impact of Lorentz invariance violation (LIV) on radiation processes in astrophysical sources, focusing on synchrotron and inverse Compton interactions. We derive modified expressions for radiated power and photon energy under LIV assumptions and incorporate them into first-order Fermi acceleration models. Our analysis reveals energy thresholds beyond which LIV significantly alters particle dynamics and photon spectra, introducing non-physical divergences that highlight limitations in perturbative approaches. We model synchrotron self-Compton (SSC) emission in the presence of LIV and assess its consequences for photon fluxes from blazars, including Markarian 501 and the BL Lac population. LIV introduces distinct high-energy emission regions that deviate from standard expectations. Comparisons with observational data, particularly upper limits from the Pierre Auger Observatory, suggest that future multi-messenger observations could constrain LIV parameters through the non-detection of such excesses.

Contents

1	Introduction	1
2	LIV framework	2
3	Radiation processes in particle acceleration under LIV assumption	3
3.1	Synchrotron radiation under LIV assumption	3
3.2	Inverse Compton under LIV assumption	4
4	First-order Fermi acceleration including radiation process under LIV assumption	5
4.1	Synchrotron radiation in first-order Fermi acceleration under LIV assumption	5
4.1.1	Synchrotron: maximum energy of accelerated particles	6
4.1.2	Synchrotron: energy spectrum of particles and photons	6
4.2	Synchrotron self-Compton in first-order Fermi acceleration under LIV assumption	7
4.2.1	Synchrotron self-Compton: energy spectrum of particles and photons	8
5	Radiation emission from blazars	8
5.1	GeV-TeV photon flux from Markarian 501	8
5.2	Ultra-high energy photons from BL Lac	9
6	Conclusion	10

1 Introduction

Lorentz invariance (LI) is a fundamental principle in modern physics, underlying the theory of relativity [1] and the standard model of particle physics [2, 3]. It asserts that the laws of physics remain the same across all frames of reference. However, potential violations of Lorentz invariance (LIV) [4] have been theorized within the context of quantum gravity [5–7] and other theories beyond the standard model [8, 9]. Investigating these possible violations provides insight into fundamental aspects of the universe, potentially revealing new physics at extremely high energies.

The propagation of astroparticles in the Universe [10–14] and in the development of extensive air showers [15, 16] have imposed limits on LIV parameters [17–21]. Nonetheless, a thorough investigation of the processes leading to the production of charged particles and photons under the hypothesis of LIV remains necessary [22].

The mechanisms generating these particles and photons are fundamentally dependent on LI, which plays a critical role in determining the maximum energy, the emitted power, and the resulting energy spectrum [23]. Consequently, such sources provide a natural framework for probing potential modifications of LI. In particular, the detection

of highly energetic astroparticles accompanied by photon counterparts offers a promising framework for probing potential deviations from LI within the context of multi-messenger astrophysics.

In this work, we investigate how LIV changes synchrotron and inverse Compton [24] interactions, the two most important energy loss processes in astrophysical sources [25–31]. We also incorporate the LIV models for synchrotron and inverse Compton interactions into the context of first-order Fermi acceleration and photon emission in blazars. We investigate how the production of high-energetic particles and photons is affected by LIV assumption.

In Section 2, we present the LIV framework. In Subsection 3.1, we derive the expressions for the LIV-modified synchrotron radiated power and the corresponding synchrotron photon energy. The application of LIV to the inverse Compton scattering process is addressed in Subsection 3.2. A combined treatment of synchrotron and inverse Compton emission within a synchrotron self-Compton (SSC) scenario, incorporating LIV effects, is developed in Section 4, where we analyze a case study of first-order Fermi acceleration. In this context, we independently evaluated the impact of LIV on both energy losses and energy spectrum of particles, as well as on the resulting photon emission. Section 5 presents a comparison between our theoretical predictions and observational data, including the identified blazar population and upper limits on photon flux from the Pierre Auger Observatory. Finally, our conclusions and implications are summarized in Section 6.

2 LIV framework

Lorentz Invariance Violation (LIV), as predicted by various theoretical models [32–34], leads to a modification of Einstein’s energy-momentum dispersion relation. This deviation can be expressed by additional terms in the standard dispersion relation:

$$E^2 = m^2 + p^2 + \sum_n \delta_n p^{n+2}, \quad (2.1)$$

where we have set $c = 1$. The momentum coefficients δ_n represent the parameters responsible for the strength of LIV, while n denotes the order of violation. Considering that we focus on highly energetic particles, we assume $p \gg m$ which leads to

$$p = \frac{E}{\sqrt{1 + \delta_n E^n}}. \quad (2.2)$$

Lorentz Invariance Violation will also modify the Lorentz factor, and, as shown in Reference [35], this shall be done via the group velocity. Considering the definition $\gamma^2 = (1 - v^2)^{-1}$, as well as the group velocity, $v = \frac{\partial E}{\partial p}$, the LIV-modified Lorentz factor results in

$$\gamma_{\text{LIV}}^2 = \frac{E^2}{m^2 - (n + 1) \delta_n E^{n+2}}, \quad (2.3)$$

where the high-energy approximation was used. As can be observed, the Lorentz factor increases even faster with energy under the LIV assumption and tends to infinity when

$E^{n+2} \rightarrow \frac{m^2}{(n+1)\delta_n}$. Once this occurs, the Lorentz factor becomes negative, revealing a fundamental limitation of the current model and indicating the need for a non-perturbative treatment.

Different particles may exhibit different breaking parameters [4], therefore we will denote the breaking parameters for electrons as $\delta_n^{(e)}$, for protons as $\delta_n^{(p)}$ and for photons as $\delta_n^{(\gamma)}$. When δ_n is used, without specifying the type of particle, a charged particle is being considered.

3 Radiation processes in particle acceleration under LIV assumption

Accelerated charged particles emit electromagnetic radiation as described by Larmor's formula [23, 36, 37]. The emitted power is

$$P = \frac{2}{3}q^2\gamma^6 \left[|\dot{\vec{v}}|^2 - |\vec{v} \times \dot{\vec{v}}|^2 \right], \quad (3.1)$$

where q is the charge of the particle, v and γ are respectively its velocity and its Lorentz factor in the laboratory frame of reference. In the next subsections we solve synchrotron and inverse Compton radiation considering LIV.

3.1 Synchrotron radiation under LIV assumption

A charged particle moving with velocity \vec{v} through a magnetic field (\vec{B}) is subject to the Lorentz force, $\vec{F} = q\vec{v} \times \vec{B}$. This acceleration results in the emission of electromagnetic radiation, a process known as synchrotron radiation. Given that the force is always perpendicular to the velocity $\vec{F} = q\vec{v} \times \vec{B} = \gamma m \dot{\vec{v}}$, the power emitted in synchrotron radiation is

$$P = \frac{2}{3} \frac{q^4}{m^2} \gamma^2 |\vec{v} \times \vec{B}|^2. \quad (3.2)$$

The energy of the emitted photons is highly concentrated at the peak of the spectral power distribution [38]. For simplicity, we assume the charged particle emits all photons with the same energy at the peak frequency

$$E_\gamma = 0.29 \cdot \frac{3}{2} \gamma^2 \frac{qB}{m}. \quad (3.3)$$

Using equation 3.4

$$P^{\text{LIV}} = \frac{2}{3} \frac{q^4}{m^4} |\vec{v} \times \vec{B}|^2 \left[\frac{E^2}{1 - (n+1) \frac{\delta_n}{m^2} E^{n+2}} \right] \quad (3.4)$$

and

$$E_\gamma^{\text{LIV}} = 0.29 \cdot \frac{3}{2} \cdot \frac{qB}{m^3} \left[\frac{E^2}{1 - (n+1) \frac{\delta_n}{m^2} E^{n+2}} \right]. \quad (3.5)$$

LIV has a significant effect on the synchrotron radiation. The modification of the Lorentz factor leads to a discontinuity at $E^{n+2} = \frac{m^2}{(n+1)\delta_n}$ in the power emitted and energy of the

emitted photons. For particles with energy $E^{n+2} > \frac{m^2}{(n+1)\delta_n}$, the energy of the emitted photon becomes negative. These consequence of the calculations indicates a limitation in the perturbative approach used here. Introducing new physics for scales beyond the breaking point may be necessary to fully describe such events. Similar consequences were obtained by different approaches [39, 40].

3.2 Inverse Compton under LIV assumption

Inverse Compton scattering is the interaction in which a low-energy photon gains energy by scattering off a high-energy charged particle. The energy of the scattered photon can be calculated imposing the conservation of the Lorentz-invariant 4-momentum

$$p_p^\mu + p_\gamma^\mu = p_p'^\mu + p_\gamma'^\mu, \quad (3.6)$$

where p denotes the charged particle, γ denotes photon and primed quantities refer to final states.

The scattering cross section of relativistic particles is given by the Klein-Nishina formula [24]

$$\sigma_{\text{KN}} = \frac{r_e^2}{2} \int \left(\frac{E'_\gamma}{E_\gamma} \right)^2 \left(\frac{E'_\gamma}{E_\gamma} + \frac{E_\gamma}{E'_\gamma} - \sin^2 \theta \right) d\Omega, \quad (3.7)$$

and the average scattering angle can be calculate through

$$\langle \cos \theta \rangle = \frac{\int \cos \theta \frac{d\sigma}{d\Omega} d\Omega}{\int \frac{d\sigma}{d\Omega} d\Omega}. \quad (3.8)$$

Introducing LIV via the energy-momentum in Equation 2.1, the spatial components ($\mu = 1, 2, 3$) become

$$E_p'^2 = m^2 + \left(\frac{E_\gamma'^2}{1 + \delta_n^{(\gamma)} E_\gamma'^n} + \frac{E_\gamma^2}{1 + \delta_n^{(\gamma)} E_\gamma^n} - \frac{2E_\gamma E_\gamma' \cos \theta}{\sqrt{(1 + \delta_n^{(\gamma)} E_\gamma'^n) (1 + \delta_n^{(\gamma)} E_\gamma^n)}} \right) \times \left[1 + \delta_n \left(\frac{E_\gamma'^2}{1 + \delta_n^{(\gamma)} E_\gamma'^n} + \frac{E_\gamma^2}{1 + \delta_n^{(\gamma)} E_\gamma^n} - \frac{2E_\gamma E_\gamma' \cos \theta}{\sqrt{(1 + \delta_n^{(\gamma)} E_\gamma'^n) (1 + \delta_n^{(\gamma)} E_\gamma^n)}} \right)^{n/2} \right]^{1/2}, \quad (3.9)$$

where θ is the scattering angle, while the time component ($\mu = 0$) yields

$$m^2 + 2mE_\gamma + E_\gamma^2 - E_\gamma'^2 - E_p'^2 - 2E_\gamma E_p' = 0. \quad (3.10)$$

Reference [41] showed similar results for the case $n = 1$, however here were present a generalization for all values of n . For this interaction, LIV effects could be considered

in the charged particle sector and the photon sector. In the following, we focus on the photon sector and defer the full treatment of charged-particle sector to a future work.

We set $\delta_n = 0$ to isolate effects on the photon sector and solved Equation 3.10 numerically. Figure 1 shows the LIV effect on the energy of the photon after the interaction. The plot shows how the energy of the photon after the interaction (final photon energy) depends on the the energy of the photon before the interaction (initial photon energy) for different LIV coefficients. The energy of the photon after the interaction tends to the Thomson regime when the initial photon energy is larger than a value depending on the LIV coefficient as shown in the plot. This can be verified as Equation 3.9 and Equation 3.10 leads to $E'_\gamma = E_\gamma$, which is the Thomson regime, in the high-energy limit ($\delta_n^{(\gamma)} E_\gamma^n \gg 1$).

Figure 2 shows the evolution of the cross section with the initial energy of the photon including LIV via Equations 3.9 and 3.10. LIV significantly impacts σ_{KN} , enhancing the interaction probability and effectively bypassing Klein-Nishina suppression until the Thomson limit is recovered.

Figure 3 shows the evolution of the scattering angle with the initial energy of the photon including LIV. A new transition to the Thomson regime is observed at high energies.

Using the modified cross section and final energy of the photon, the emitted power under LIV assumption can be calculated via

$$P = \int \sigma_{\text{KN}} [E'_\gamma - E_\gamma] \eta(E_\gamma) dE_\gamma, \quad (3.11)$$

where $\eta(E_\gamma)$ is the energy distribution of photons before the interaction. LIV increases both the final energy and cross section, thus amplifying the emitted power.

4 First-order Fermi acceleration including radiation process under LIV assumption

First-order Fermi mechanism [42–44] is an efficient acceleration process known to be working in several astrophysical sources. In a previous publication [22], we investigated how LIV modifies the energy gain per scattering, the acceleration timescales, and the spectral indices of particles accelerated by the first-order Fermi mechanism. In this Section, we will merge the first-order Fermi with synchrotron and SSC energy losses, both including LIV.

4.1 Synchrotron radiation in first-order Fermi acceleration under LIV assumption

The synchrotron loss process can be highly relevant in scenarios of astrophysical particle acceleration, mainly in two stages: initially, during the acceleration of the charged particles itself, where energy gains compete with radiative losses; and subsequently, near the source, where the particles interacts with the radiation fields.

4.1.1 Synchrotron: maximum energy of accelerated particles

In Reference [22], we calculated the energy gained by a particles under first-order Fermi acceleration considering LIV. This modified energy gain, along with the power lost through synchrotron radiation, gives the following net gain, $-b$:

$$b = -\frac{\langle \Delta E \rangle}{\tau_{avg}} + P_{sync} \frac{\tau_{avg}}{\tau_{avg}}, \quad (4.1)$$

where τ_{avg} is the average crossing time for the particle traversing the shock wave. We consider the best case scenario of Bohm diffusion [45]

$$\tau_{avg} \approx \frac{5}{qBV} \frac{E}{\sqrt{1 + \delta_n E^n}}. \quad (4.2)$$

In a scenario where synchrotron radiation is the dominant energy loss during shock wave acceleration, we can use Equation 3.4 to determine the maximum energy a charged particle can gain through first-order Fermi acceleration [46] as the equilibrium between loss and energy gain, $\langle \Delta E \rangle = P_{sync} \cdot \tau_{avg}$, which gives

$$\frac{E_{max}^2}{[1 - (n+1) \frac{\delta_n}{m^2} E^{n+2}]} \approx \frac{m^4}{B}. \quad (4.3)$$

Figure 4 and Figure 5 shows the solution to this equation as a function of δ_n for electrons and protons, respectively. A transition between two regimes is very clear. In the regime of low δ_n values, the maximum energy is determined by the balance between energy gain and synchrotron losses. As δ_n increases, LIV becomes more significant, the Lorentz factor barrier dominates, such that a particle reaching $E^{n+2} = \frac{m^2}{(n+1)\delta_n}$ would emit all its energy, as shown in Equation 3.4. This transition is shown as an abrupt energy loss in these plots.

4.1.2 Synchrotron: energy spectrum of particles and photons

We will use the one-zone model to calculate the energy spectrum of particle accelerated in the source [47]. This model considers particles traveling through an acceleration and a cooling (or energy-loss) region. The transport of particles can be calculate using the diffusion-loss equation to describe the number of particles N within an energy range E to $E + \delta E$ at a given time

$$\frac{dN}{dt} + \frac{d}{dE} [b \cdot N] = -\frac{N}{\tau_{scp}} + Q_{inj}, \quad (4.4)$$

where b is the energy loss rate in this case dominated by synchrotron radiation, τ_{esc} is the escape timescale from the cooling region (here neglected), and $Q_{inj}(E)$ is the injection spectrum from the acceleration site. We model Q_{inj} as a first-order Fermi spectrum with LIV and an exponential cutoff at E_{max} (derived in Subsection 4.1.1).

Figures 6 and 7 show the energy spectrum of charged particles resulting from the one-zone model including LIV for electrons and protons, respectively. A magnetic field of

$B = 10^{-10}$ T was used. The suppression in the energy spectrum is a direct consequence of the barrier created by the Lorentz factor. As shown in section 4.1.1, above a certain maximum energy which depends on the LIV break, energy losses are dominant and particles stop gaining energy.

The energy spectrum of photons produced by the accelerated particles via synchrotron emission can be modeled by [23]

$$N_\gamma(E_\gamma) = \frac{D}{4\pi} \int_{E_{min}}^{E_{max}} P(E) N_p(E) dE, \quad (4.5)$$

where P is the synchrotron power, N_p is the particle's energy spectrum and D is the volume of the source. As previously discussed, we assume all photons are emitted with the same energy at the peak frequency, resulting in

$$N_\gamma(E_\gamma) \approx 10^{14} \frac{DB}{m} N_p(E) E \left[\frac{1 - (n+1) \frac{\delta_n}{m^2} E^{n+2}}{1 + (n+1)^2 \frac{\delta_n}{m^2} E^{n+2}} \right], \quad (4.6)$$

where E is the energy of the particle that emits a photon with energy E_γ according to Equation 3.5 and $N_p(E)$ is the spectrum calculated using Equation 4.4.

Figures 8 and 9 shows the resulting energy spectrum for electrons and protons, respectively. In this calculations, we considered a source with the size 1 pc.

LIV leads to the emergence of a distinct high-energy emission, where the final photon energy exhibits rapid growth near the divergence threshold - $E^{n+2} \rightarrow \frac{m^2}{(n+1)\delta_n}$ - expected from Equation 3.5. Notably, this region contributes a non-negligible flux, consistent with the increasing emitted power derived in Equation 3.4. However, it is important to note that the energy of the emitted photon exceeds that of the electron or proton responsible for its production, thus violating energy conservation. The energy range where this violation occurs is indicated by a dashed line in Figures 8 and 9.

Lorentz invariance violation not only introduces an unanticipated energy domain in synchrotron emission but could also alter SSC spectra through the inclusion of higher-energy photons in the radiation background, leading to emissions at previously unexpected energies and potential alterations of the predicted spectra. These modifications could serve as a means to constrain LIV, as the non-detection of such new energy regions could impose limits on the LIV parameters.

4.2 Synchrotron self-Compton in first-order Fermi acceleration under LIV assumption

In non-thermal astrophysical spectra, the population of higher-energy photons is commonly attributed to the inverse Compton scattering. In this process, background photons near the source gain energy from charged particles in the acceleration region.

In regions with a high concentration of electrons and strong magnetic fields, the SSC model can become dominant [23, 48, 49]. In this framework, the seed photons originate from the synchrotron radiation produced by the particle population itself. This study will focus on this type of process, where the photon density in Equation 3.11 is determined

by the synchrotron emission, presented in Equation 4.6, while the cross section and final photon energy are the same discussed in Subsection 3.2. Notice that $\delta_n^{(\gamma)}$ will not affect the photon distribution, only the inverse Compton scattering will be affected by this parameter. Again, the parameter δ_n will be set to 0 in order to focus exclusively on the behavior of LIV in photons.

4.2.1 Synchrotron self-Compton: energy spectrum of particles and photons

In this section, we repeat the calculations of in Subsection 4.1.2 now considering SSC as the dominant energy-loss mechanism. Figures 10 and 11 shows the energy spectrum of electrons and protons, respectively. A suppression of the flux with increasing energy is seen in both cases. The suppression caused by LIV is well below in energy and has less abrupt fall when compared to the cutoff in SSC under LI assumption. The LIV suppression is caused by two effects, the final energy in the interaction and the cross section, which tend to increase rapidly when LIV is considered, inducing a growth in the emitted power.

Following the same arguments of previous section, we also calculated the energy spectrum of photons produced in SSC interaction of the charged particles. Figure 12 and 13 shows the energy spectrum of photons resulting from the interaction of electrons and protons, respectively. A magnetic field of $B = 10^{-10}$ T was considered.

The photons emitted by protons and electrons exhibit similar behavior, differing primarily in their LIV parameters due to the proton's higher energy. As shown in Figures 12 and 13, a new emission region emerges at higher energies due to LIV. The peak height depends on the magnetic field strength, with stronger fields producing more energetic background photons, enhancing LIV effects. The charged-particle cutoff energy also influences emission in this region — lower cutoffs reduce its prominence. We assume SSC losses dominate, significantly suppressing the particle energy spectrum (Figures 10, 11), therefore, a competition arises between Fermi-accelerated spectral shaping and emission effects: a stronger violation increases emission but suppresses the electron/proton population responsible for high-energy photons. This suppression also shifts the standard SSC peak to lower energies. In contrast, for systems that are dominated by synchrotron losses - Figure 14 - only emission modifications persist without spectral suppression.

5 Radiation emission from blazars

In the previous sections, idealized cases of acceleration, emission, and related processes were considered to highlight the new LIV phenomena introduced in each case. In this section we explore a more realistic scenario of photon production including LIV in Markarian 501 and in blazars.

5.1 GeV-TeV photon flux from Markarian 501

We used the models developed in the previous sections to calculate the GeV-TeV photon flux generated in Mkr 501. We used the data reference [50], in particular the magnetic field strength and the electron energy spectrum responsible for both synchrotron emission

and the inverse Compton process. We assume a cutoff at 10^{14} eV, consistent with the maximum energy predicted by Equation 4.3 under the magnetic field conditions of Mrk 501.

Figure 15 shows the energy spectrum of photons for two values of LIV break when synchrotron emission is considered according to section 3.1. The emission extends to higher energies, effectively bypassing the cutoff imposed by the LI predictions. Additionally, Figure 16, which presents a magnified view of the synchrotron peak, shows that for sufficiently large LIV parameters, even the low-energy portion of the spectrum may be altered, leading to a noticeable divergence from the observational data.

Figure 17 shows the energy spectrum of photons for two values of LIV break when SSC emission is considered according to section 3.2. A second emission region is predicted under LIV assumption which is not present in LI models. This new component in the flux allows open a new window to constrain the parameters associated with LIV. The non-detection of the predicted high-energy photons would impose upper limits on the extent of the violation.

5.2 Ultra-high energy photons from BL Lac

The new emission regions arising from synchrotron and SSC processes also populate the photon spectrum at energies above 10^{17} eV.

To illustrate this possibility, we compare the predicted LIV-induced emissions with the upper limits on the photon flux established by the Pierre Auger Observatory [51, 52]. The flux is modeled as originating from a population of BL Lac objects, given that approximately 10^3 such sources have been identified [53, 54]. For simplicity, the combined flux is computed by summing the contributions of 10^3 identical sources, without accounting for source distribution, propagation effects, or intrinsic source-to-source variations, and adopting typical parameters for BL Lac objects [55]. We note that the determination of average source parameters typically does not aim to constrain the cutoff energy of the electron energy spectrum, as its impact on the overall source characteristics is minimal. Therefore, in this work we adopt a cutoff energy of 10^{14} eV.

Figures 18 and 19 shows the energy spectrum of synchrotron photons calculated with this simplified model considering LIV for $n = 1$ and $n = 2$, respectively. We show the upper limits on the photons flux measured by the the Pierre Auger Observatory for comparison in Figures 20 and 21.

A similar procedure was applied to the SSC emission considering LIV. The energy spectrum of photons are presented in Figures 22 and 23 for $n = 1$ and $n = 2$, respectively. Additionally, we consider a scenario without an intrinsic cutoff in the electron energy distribution, illustrating the most optimistic case for high-energy photon emission. These comparisons between the flux and the Pierre Auger Observatory limits can be seen in Figures 24 and 25.

At present, the comparison with Pierre Auger data does not yield constraints on the LIV parameters investigated. Establishing meaningful limits would require a more detailed astrophysical treatment, including the effects of source distribution, cosmological propagation, and potential contributions from other classes of sources, such as flat-

spectrum radio quasars. Increasing the number of detected sources would enhance the cumulative photon flux, and a detailed analysis incorporating these effects could potentially lead to significant constraints on LIV.

6 Conclusion

In this work, we examined the influence of Lorentz invariance violation (LIV) on the production and emission of high-energy particles and photons in astrophysical environments. By modifying synchrotron and inverse Compton processes within the LIV framework, we derived the resulting changes in radiated power, photon energy, and energy spectra of accelerated particles. Our results demonstrate that LIV induces a rapid growth in the Lorentz factor at high energies, leading to divergences in emission characteristics and suggesting a breakdown of the perturbative formalism, requiring new theoretical treatments at extreme energies.

Incorporating these effects into first-order Fermi acceleration models and synchrotron self-Compton scenarios, we showed that LIV modifies both particle spectra and the resulting multi-wavelength photon emission. In particular, LIV predicts the emergence of distinct high-energy components in the photon spectrum that are absent under Lorentz-invariant assumptions. These features were evaluated in astrophysical study cases, including the GeV–TeV emission from Markarian 501 and ultra-high-energy photons from a population of BL Lac objects.

While current observational data, such as the upper limits from the Pierre Auger Observatory, do not yet constrain the explored LIV parameters, our results demonstrate that astrophysical photon spectra provide a promising avenue for probing violations of Lorentz symmetry. Future multi-messenger observations, with improved sensitivity to both particle and photon fluxes, may offer critical tests of fundamental symmetries at the highest energies.

Acknowledgments

The authors are supported by the São Paulo Research Foundation (FAPESP) through grant number 2021/01089-1. VdS is supported by CNPq through grant number 308837/2023-1. MDF is supported by CAPES through grant number 88887.684414/2022-00. The authors acknowledge the National Laboratory for Scientific Computing (LNCC/MCTI, Brazil) for providing HPC resources for the SDumont supercomputer (<http://sdumont.lncc.br>).

References

- [1] A. Einstein, *Zur Elektrodynamik bewegter Körper*, *Annalen Phys.* **17** (1905) 891.
- [2] M.K. Gaillard, P.D. Grannis and F.J. Sciulli, *The standard model of particle physics*, *Reviews of Modern Physics* **71** (1999) S96–S111 [[hep-ph/9812285](#)].
- [3] PARTICLE DATA GROUP collaboration, *Review of Particle Physics*, *PTEP* **2022** (2022) 083C01.

- [4] D. Mattingly, *Modern Tests of Lorentz Invariance*, *Living Reviews in Relativity* **8** (2005) [[gr-qc/0502097](#)].
- [5] R. Alves Batista et al., *White Paper and Roadmap for Quantum Gravity Phenomenology in the Multi-Messenger Era*, [2312.00409](#).
- [6] A. Addazi et al., *Quantum gravity phenomenology at the dawn of the multi-messenger era—A review*, *Prog. Part. Nucl. Phys.* **125** (2022) 103948 [[2111.05659](#)].
- [7] A. Ashtekar and E. Bianchi, *A short review of loop quantum gravity*, *Rept. Prog. Phys.* **84** (2021) 042001 [[2104.04394](#)].
- [8] O.W. Greenberg, *CPT Violation Implies Violation of Lorentz Invariance*, *Phys. Rev. Lett.* **89** (2002) 231602 [[hep-ph/0201258](#)].
- [9] A.E. Bernardini and O. Bertolami, *Lorentz violating extension of the Standard Model and the beta-decay end-point*, *Phys. Rev. D* **77** (2008) 085032 [[0802.2199](#)].
- [10] J.M. Carmona, J.L. Cortés, F. Rescic, M.A. Reyes, T. Terzić and F.I. Vrban, *Approaches to photon absorption in a Lorentz invariance violation scenario*, *Phys. Rev. D* **110** (2024) 063035 [[2404.07842](#)].
- [11] G. Amelino-Camelia, J.R. Ellis, N.E. Mavromatos, D.V. Nanopoulos and S. Sarkar, *Tests of quantum gravity from observations of gamma-ray bursts*, *Nature* **393** (1998) 763 [[astro-ph/9712103](#)].
- [12] U. Jacob and T. Piran, *Lorentz-violation-induced arrival delays of cosmological particles*, *Journal of Cosmology and Astroparticle Physics* **2008** (2008) 031 [[0712.2170](#)].
- [13] M. Schreck, *Vacuum Cherenkov radiation for Lorentz-violating fermions*, *Physical Review D* **96** (2017) [[1702.03171](#)].
- [14] S. Zhang and B.-Q. Ma, *Lorentz violation from gamma-ray bursts*, *Astroparticle Physics* **61** (2015) 108–112 [[1406.4568](#)].
- [15] A. Saveliev and R. Alves Batista, *Simulating electromagnetic cascades with Lorentz invariance violation*, *Class. Quant. Grav.* **41** (2024) 115011 [[2312.10803](#)].
- [16] F. Duenkel, M. Niechciol and M. Risse, *Photon decay in ultrahigh-energy air showers: Stringent bound on Lorentz violation*, *Physical Review D* **104** (2021) [[2106.01012](#)].
- [17] H. Martínez-Huerta, R.G. Lang and V. de Souza, *Lorentz Invariance Violation Tests in Astroparticle Physics*, *Symmetry* **12** (2020) .
- [18] P. Satunin, *New constraints on Lorentz Invariance violation from Crab Nebula spectrum beyond 100 TeV*, *The European Physical Journal C* **79** (2019) [[1906.08221](#)].
- [19] A. Albert, R. Alfaro, C. Alvarez, J. Angeles Camacho, J. Arteaga-Velázquez, K. Arunbabu et al., *Constraints on Lorentz Invariance Violation from HAWC Observations of Gamma Rays above 100 TeV*, *Physical Review Letters* **124** (2020) [[1911.08070](#)].
- [20] V.A. Kostelecký and J.D. Tasson, *Constraints on Lorentz violation from gravitational Čerenkov radiation*, *Physics Letters B* **749** (2015) 551–559 [[1508.07007](#)].
- [21] THE PIERRE AUGER collaboration, *Testing effects of Lorentz invariance violation in the propagation of astroparticles with the Pierre Auger Observatory*, *Journal of Cosmology and Astroparticle Physics* **2022** (2022) 023 [[2112.06773](#)].
- [22] M. Duarte and V. de Souza, *Fermi acceleration under Lorentz invariance violation*, *JCAP* **10** (2024) 029 [[2407.17254](#)].

- [23] G. Ghisellini, *Radiative Processes in High Energy Astrophysics*, Springer International Publishing (2013), [10.1007/978-3-319-00612-3](https://doi.org/10.1007/978-3-319-00612-3).
- [24] O. Klein and Y. Nishina, *Über die Streuung von Strahlung durch freie Elektronen nach der neuen relativistischen Quantendynamik von Dirac*, *Z. Phys.* **52** (1929) 853.
- [25] C. Ridgers, J. Kirk, R. Ducloux, T. Blackburn, C. Brady, K. Bennett et al., *Modelling gamma-ray photon emission and pair production in high-intensity laser–matter interactions*, *Journal of Computational Physics* **260** (2014) 273 [[1311.5551](https://arxiv.org/abs/1311.5551)].
- [26] D.-X. Sun, P.-P. Zhang, Y.-Q. Guo, W. Liu and Q. Yuan, *Multi-messenger observations support cosmic ray interactions surrounding acceleration sources*, [2307.02372](https://arxiv.org/abs/2307.02372).
- [27] M. Ruszkowski and C. Pfrommer, *Cosmic ray feedback in galaxies and galaxy clusters: A pedagogical introduction and a topical review of the acceleration, transport, observables, and dynamical impact of cosmic rays*, *Astron. Astrophys. Rev.* **31** (2023) 4 [[2306.03141](https://arxiv.org/abs/2306.03141)].
- [28] M.S. Longair, *High Energy Astrophysics*, Cambridge University Press, 3 ed. (2011), <https://doi.org/10.1017/CBO9780511778346>.
- [29] M. Pfützner, I. Mukha and S. Wang, *Two-proton emission and related phenomena*, *Prog. Part. Nucl. Phys.* **132** (2023) 104050 [[2304.13391](https://arxiv.org/abs/2304.13391)].
- [30] Lenain, J.-P., Boisson, C., Sol, H. and Katarzyński, K., *A synchrotron self-Compton scenario for the very high energy γ -ray emission of the radiogalaxy M87 - Unifying the TeV emission of blazars and other AGNs?*, *A&A* **478** (2008) 111.
- [31] T. Wen, Y.-H. Yao, S.-Z. Chen, B.-Z. Dai and Y.-Q. Guo, *A universal energy relation between synchrotron and synchrotron self-Compton radiation in GRBs and blazars*, *JHEAp* **44** (2024) 315.
- [32] J.D. Tasson, *What Do We Know About Lorentz Invariance?*, *Rept. Prog. Phys.* **77** (2014) 062901 [[1403.7785](https://arxiv.org/abs/1403.7785)].
- [33] V.A. Kostelecký, *CPT and Lorentz Symmetry*, WORLD SCIENTIFIC (2008), [10.1142/6678](https://doi.org/10.1142/6678), [<https://www.worldscientific.com/doi/pdf/10.1142/6678>].
- [34] T. Jacobson, S. Liberati and D. Mattingly, *Lorentz violation at high energy: Concepts, phenomena, and astrophysical constraints*, *Annals of Physics* **321** (2006) 150–196.
- [35] P.H. Morais, I.P. Lobo, C. Pfeifer, R. Alves Batista and V.B. Bezerra, *Modified particle lifetimes as a signature of deformed relativity*, *Phys. Lett. B* **848** (2024) 138380 [[2308.03716](https://arxiv.org/abs/2308.03716)].
- [36] J.D. Jackson, *Classical Electrodynamics*, Wiley (1998), [10.1002/3527600434.eap109](https://doi.org/10.1002/3527600434.eap109).
- [37] D.J. Griffiths, *Introduction to Electrodynamics*, Cambridge University Press, 4 ed. (2017), [10.1017/9781108333511](https://doi.org/10.1017/9781108333511).
- [38] A.G. Pacholczyk and J.A. Roberts, *Radio astrophysics: Nonthermal processes in galactic and extragalactic sources*, *Physics Today* **24** (1971) 57.
- [39] B. Altschul, *Lorentz violation and synchrotron radiation*, *Phys. Rev. D* **72** (2005) 085003 [[hep-th/0507258](https://arxiv.org/abs/hep-th/0507258)].
- [40] R. Montemayor and L.F. Urrutia, *Synchrotron radiation in Lorentz-violating electrodynamics: The Myers-Pospelov model*, *Phys. Rev. D* **72** (2005) 045018 [[hep-ph/0505135](https://arxiv.org/abs/hep-ph/0505135)].

- [41] H. Abdalla and M. Böttcher, *Lorentz Invariance Violation Effects on Gamma–Gamma Absorption and Compton Scattering*, *Astrophys. J.* **865** (2018) 159 [[1809.00477](#)].
- [42] A.R. Bell, *The acceleration of cosmic rays in shock fronts – II*, *Monthly Notices of the Royal Astronomical Society* **182** (1978) 443.
- [43] G.F. Krymskii, *A regular mechanism for the acceleration of charged particles on the front of a shock wave*, *Akademiia Nauk SSSR Doklady* **234** (1977) 1306.
- [44] R. Blandford and D. Eichler, *Particle acceleration at astrophysical shocks: A theory of cosmic ray origin*, *Physics Reports* **154** (1987) 1.
- [45] D. Bohm and E.P. Gross, *Theory of Plasma Oscillations. A. Origin of Medium-Like Behavior*, *Phys. Rev.* **75** (1949) 1851.
- [46] P. Kumar, R.A. Hernandez, Z. Bosnjak and R.B. Duran, *Maximum synchrotron frequency for shock-accelerated particles*, *Mon. Not. Roy. Astron. Soc.* **427** (2012) L40 [[1210.6033](#)].
- [47] S. Gupta, M. Boettcher and C.D. Dermer, *Time-dependent synchrotron and compton spectra from jets of microquasars*, *Astrophys. J.* **644** (2006) 409 [[astro-ph/0602439](#)].
- [48] K. Nalewajko and M. Gupta, *The sequence of Compton dominance in blazars based on data from WISE and Fermi-LAT*, *Astron. Astrophys.* **606** (2017) A44 [[1706.02308](#)].
- [49] M. Kusunose and F. Takahara, *Synchrotron Self-Compton Model for PKS 2155-304*, *Astrophys. J.* **682** (2008) 784 [[0807.3773](#)].
- [50] A. Albert et al., *Long-term Spectra of the Blazars Mrk 421 and Mrk 501 at TeV Energies Seen by HAWC*, *Astrophys. J.* **929** (2022) 125 [[2106.03946](#)].
- [51] PIERRE AUGER collaboration, *Search for photons with energies above 10^{18} eV using the hybrid detector of the Pierre Auger Observatory*, *JCAP* **04** (2017) 009 [[1612.01517](#)].
- [52] PIERRE AUGER collaboration, *Limits on ultra-high energy photons with the Pierre Auger Observatory*, *PoS ICRC2019* (2021) 398.
- [53] FERMI-LAT collaboration, *Fermi Large Area Telescope Fourth Source Catalog*, *Astrophys. J. Suppl.* **247** (2020) 33 [[1902.10045](#)].
- [54] FERMI-LAT collaboration, *Fermi Large Area Telescope Fourth Source Catalog Data Release 4 (4FGL-DR4)*, [2307.12546](#).
- [55] J. Zhang, X.-N. Sun, E.-W. Liang, R.-J. Lu, Y. Lu and S.-N. Zhang, *Relativistic Jet Properties of GeV-TeV Blazars and Possible Implications for the Jet Formation, Composition, and Cavity Kinematics*, *Astrophys. J.* **788** (2014) 104 [[1307.6911](#)].

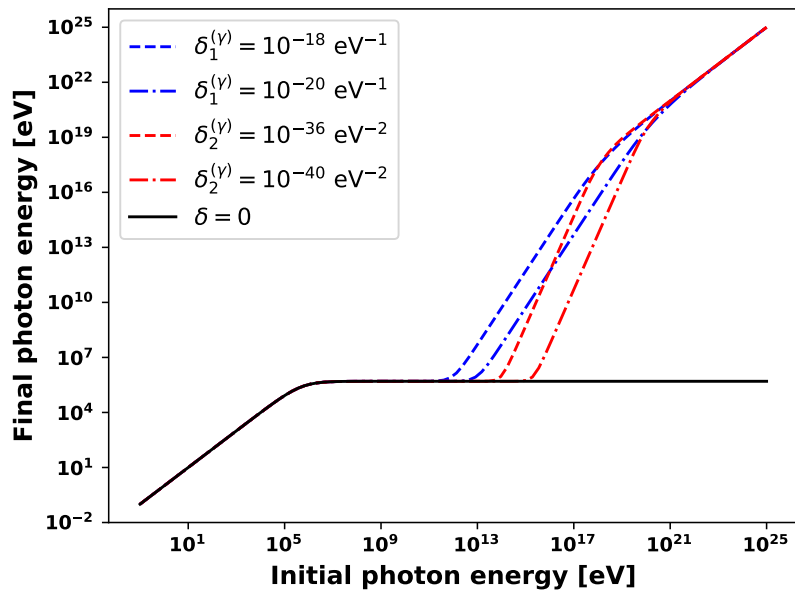


Figure 1. Final photon energy in the reference frame of the electron as a function of its initial energy. A scattering angle of $\pi/2$ was adopted. Different values of $\delta_n^{(\gamma)}$ are shown for the first two orders of violation. The electron LIV parameter was set to 0. The result for the first violation order was previously obtained in [41].

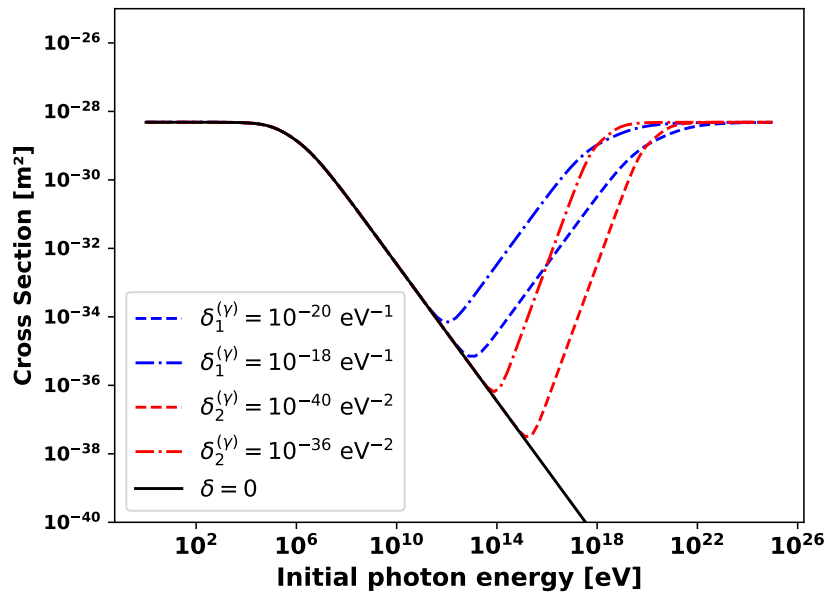


Figure 2. Klein-Nishina cross section for a photon-electron interaction. Different values of $\delta_n^{(\gamma)}$ are shown for the first two orders of violation. The electron LIV parameter was set to 0. The result for the first violation order was previously obtained in [41].

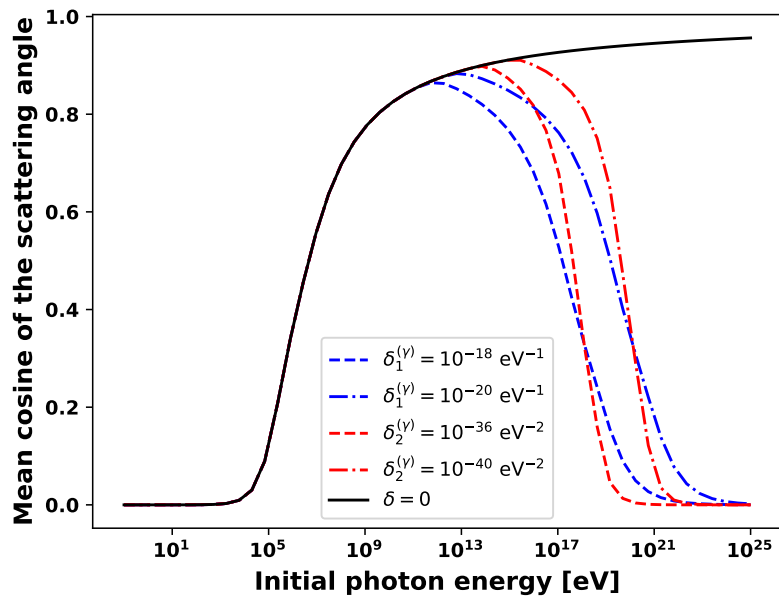


Figure 3. Average of the cosine of the scattering angle of photons as a function of the initial photon energy. Different values of $\delta_n^{(\gamma)}$ are shown for the first two orders of violation. The electron LIV parameter was set to 0.

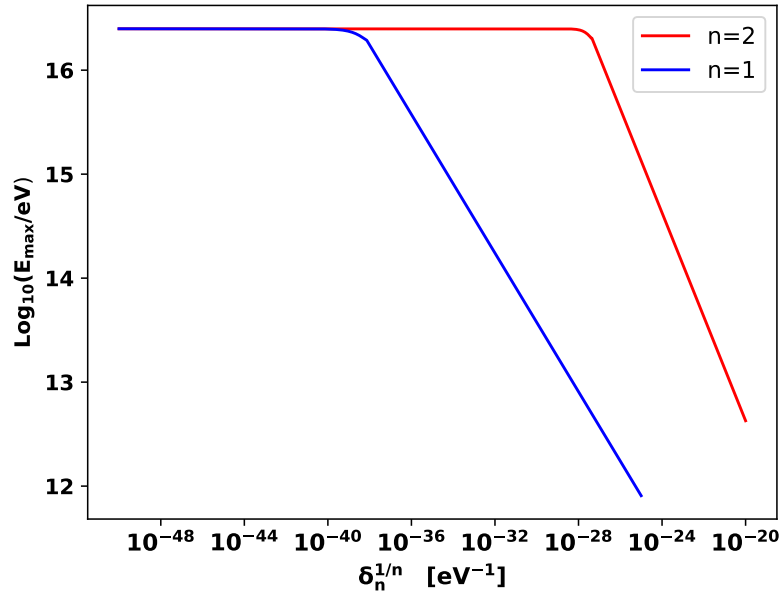


Figure 4. Maximum electron energy as a function of breaking parameter $\delta_n^{(e)}$. Electrons are accelerated via first-order Fermi mechanism and are susceptible to synchrotron losses. A magnetic field of $B = 10^{-10} T$ was adopted. Both cases of $n = 1$ and $n = 2$ are shown.

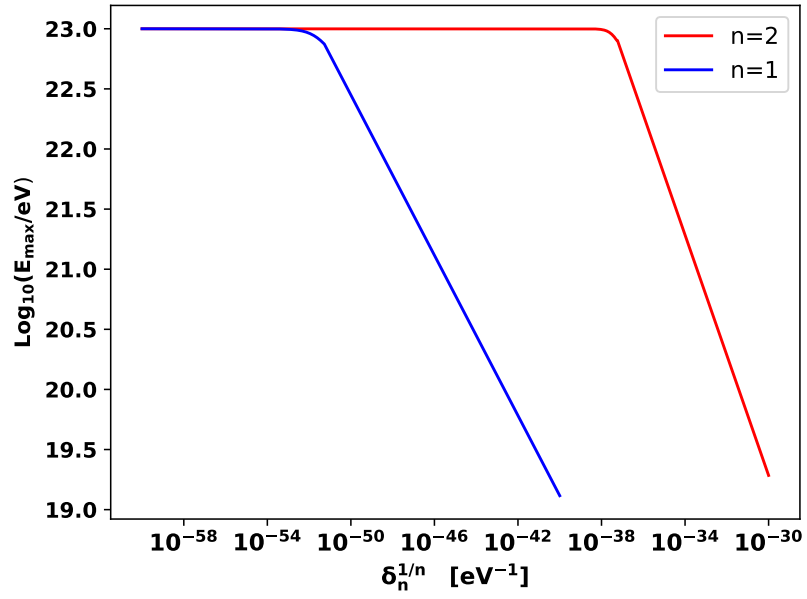


Figure 5. Maximum proton energy as a function of breaking parameter $\delta_n^{(p)}$. Protons are accelerated via first-order Fermi mechanism and are susceptible to synchrotron losses. A magnetic field of $B = 10^{-10} T$ was adopted. Both cases of $n = 1$ and $n = 2$ are shown.

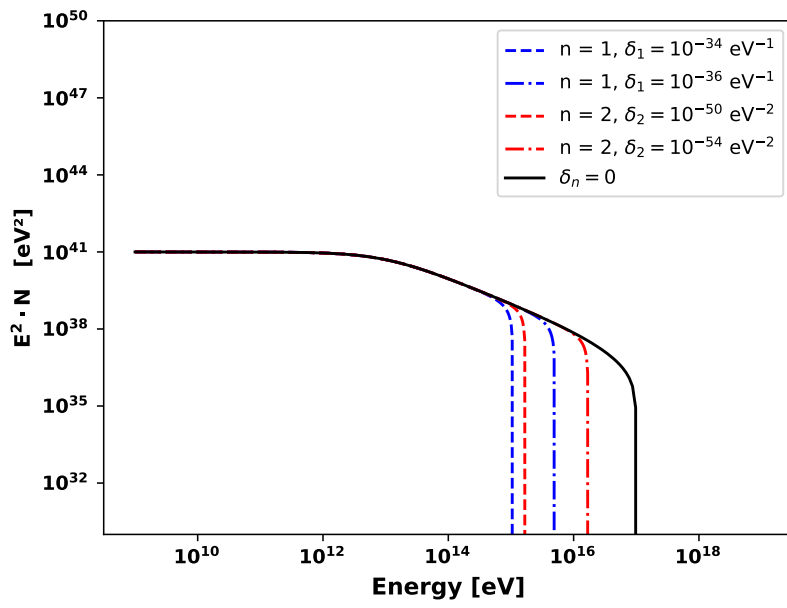


Figure 6. Electron's energy spectrum. The black solid line represents the Lorentz invariant scenario. The energy of spectral index break was taken to be $E_b = 10^{13}$ eV. Different values of $\delta_p^{(e)}$ are shown for the studied orders of violation, $n = 1$ and $n = 2$.

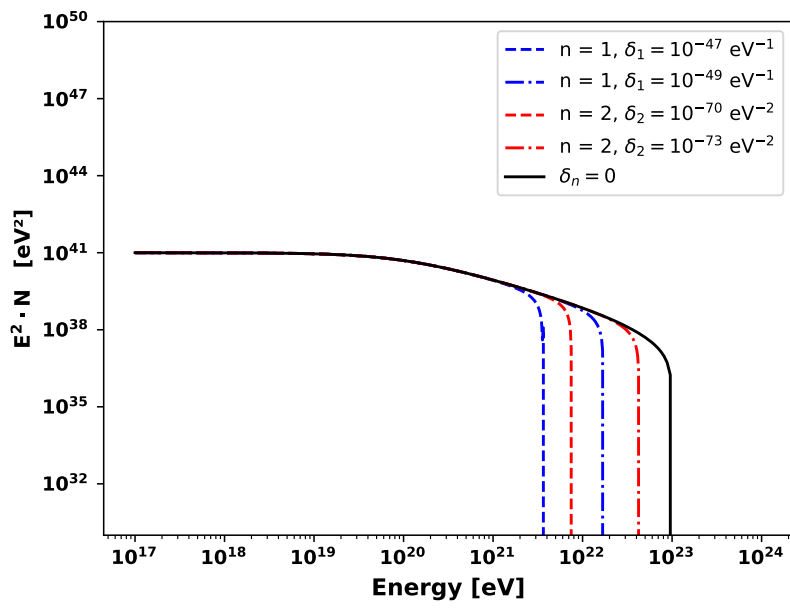


Figure 7. Proton's energy spectrum. The black solid line represents the Lorentz invariant scenario. The energy of spectral index break was taken to be $E_b = 10^{20}$ eV. Different values of $\delta_n^{(p)}$ are shown for the studied orders of violation, $n = 1$ and $n = 2$.

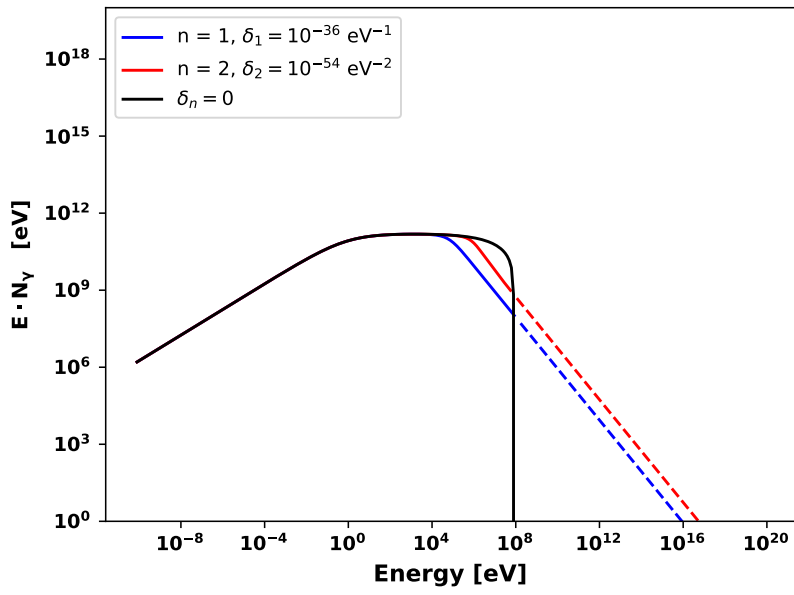


Figure 8. Photon's energy spectrum emitted via synchrotron by a population of electrons. The energy of spectral index break was taken to be $E_b = 10^{13}$ eV. A magnetic field of $B = 10^{-10}$ T was adopted. The black solid line represents the Lorentz invariant scenario. The dashed lines indicate the energy region at which energy conservation is violated. Different values of $\delta_n^{(e)}$ are shown for the studied orders of violation, $n = 1$ and $n = 2$.

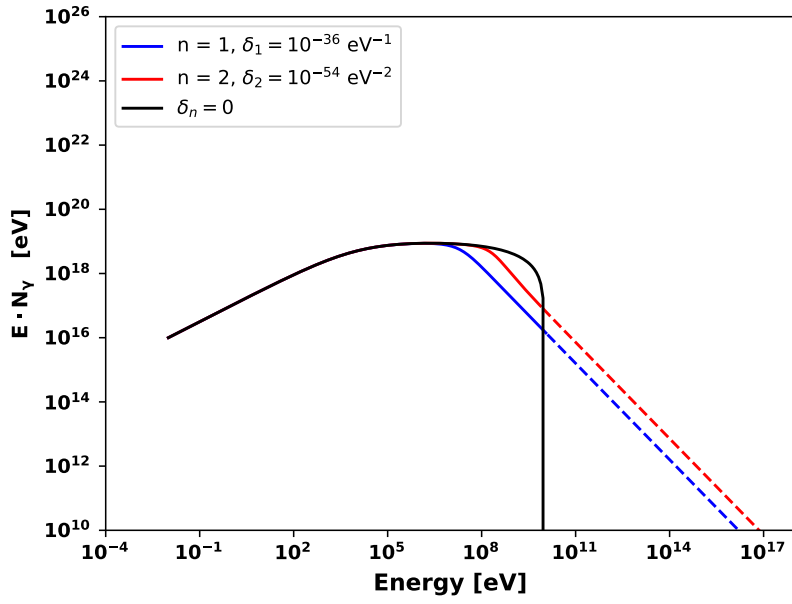


Figure 9. Photon's energy spectrum emitted via synchrotron by a population of protons. The energy of spectral index break was taken to be $E_b = 10^{20}$ eV. A magnetic field of $B = 10^{-10}$ T was adopted. The black solid line represents the Lorentz invariant scenario. The dashed lines indicate the energy region at which energy conservation is violated. Different values of $\delta_n^{(p)}$ are shown for the studied orders of violation, $n = 1$ and $n = 2$.

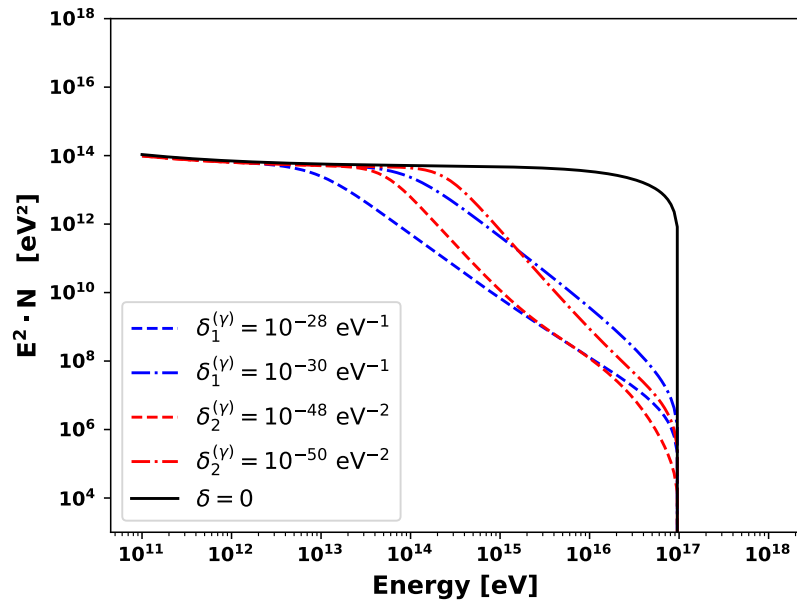


Figure 10. Electron's energy spectrum resulting from the one-zone model. The electron breaking parameter was set to 0. The energy of spectral index break was taken to be $E_b = 10^{13}$ eV. The black solid line represents the Lorentz invariant scenario. Different values of $\delta_n^{(\gamma)}$ are shown for the studied orders of violation, $n = 1$ and $n = 2$.

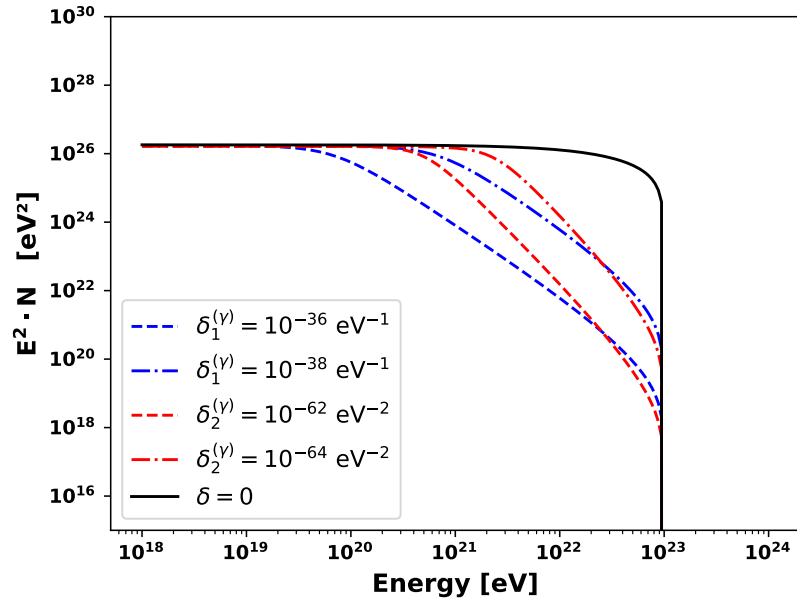


Figure 11. Proton's energy spectrum resulting from the one-zone model. The proton breaking parameter was set to 0. The energy of spectral index break was taken to be $E_b = 10^{20}$ eV. The black solid line represents the Lorentz invariant scenario. The dashed lines indicate the energy region at which energy conservation is violated. Different values of $\delta_n^{(\gamma)}$ are shown for the studied orders of violation, $n = 1$ and $n = 2$.

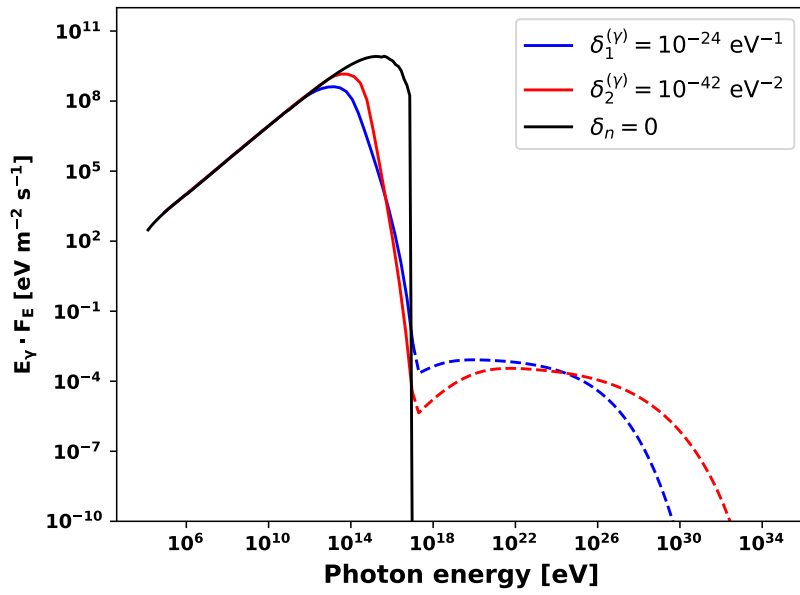


Figure 12. Photon's energy spectrum emitted via synchrotron self-Compton by a population of electrons. Inverse Compton was considered the dominant loss process. The energy of spectral index break was taken to be $E_b = 10^{11}$ eV. The black solid line represents the Lorentz invariant scenario. The dashed lines indicate the energy region at which energy conservation is violated. Different values of $\delta_n^{(\gamma)}$ are shown for the studied orders of violation, $n = 1$ and $n = 2$.

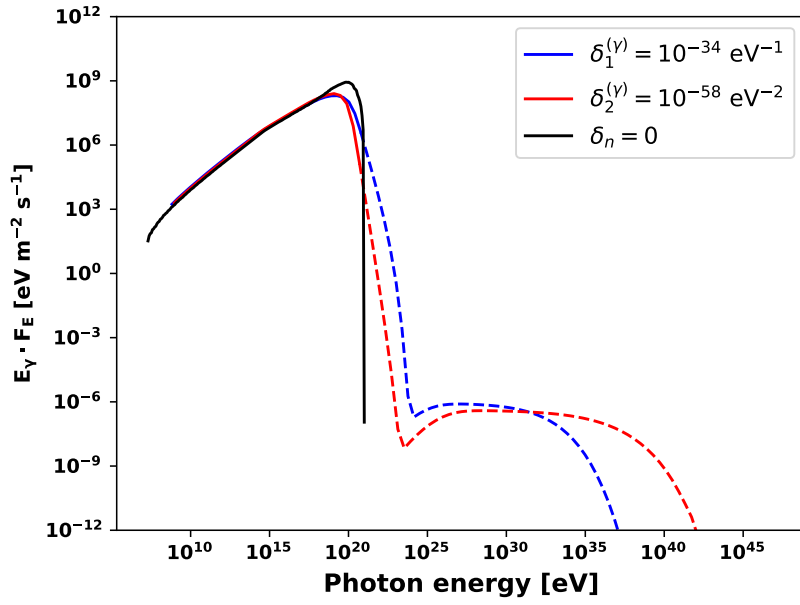


Figure 13. Photon's energy spectrum emitted via synchrotron self-Compton by a population of protons. Inverse Compton was considered the dominant loss process. The energy of spectral index break was taken to be $E_b = 10^{20}$ eV. The black solid line represents the Lorentz invariant scenario. Different values of $\delta_n^{(\gamma)}$ are shown for the studied orders of violation, $n = 1$ and $n = 2$.

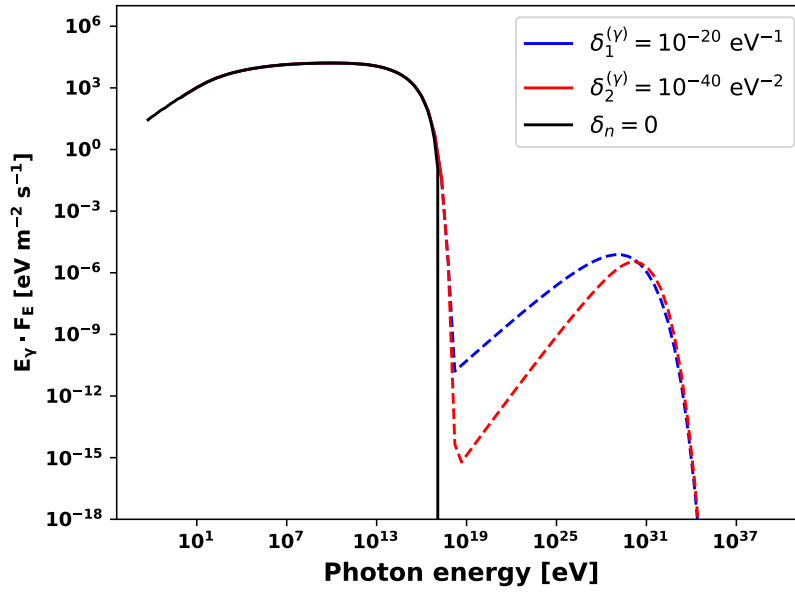


Figure 14. Photon's energy spectrum emitted via synchrotron self-Compton by a population of electrons. Synchrotron was considered the dominant loss process. The energy of spectral index break was taken to be $E_b = 10^{11}$ eV. The black solid line represents the Lorentz invariant scenario. The dashed lines indicate the energy region at which energy conservation is violated. Different values of $\delta_n^{(\gamma)}$ are shown for the studied orders of violation, $n = 1$ and $n = 2$.

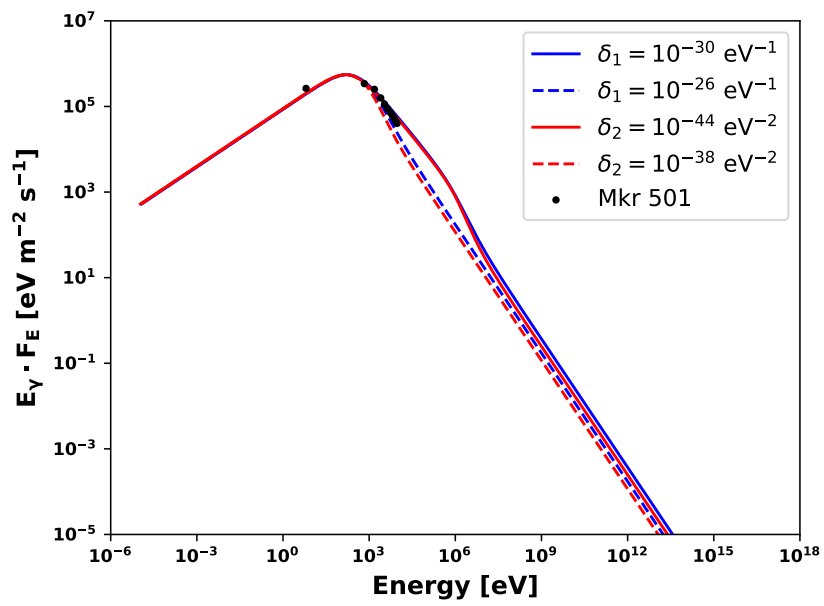


Figure 15. Photon's energy spectrum resulting from the synchrotron emission of Markarian 501. The data was taken from [19] and only the synchrotron peak is shown. Different values of $\delta_n^{(e)}$ are shown for both violation orders, $n = 1$ and $n = 2$.

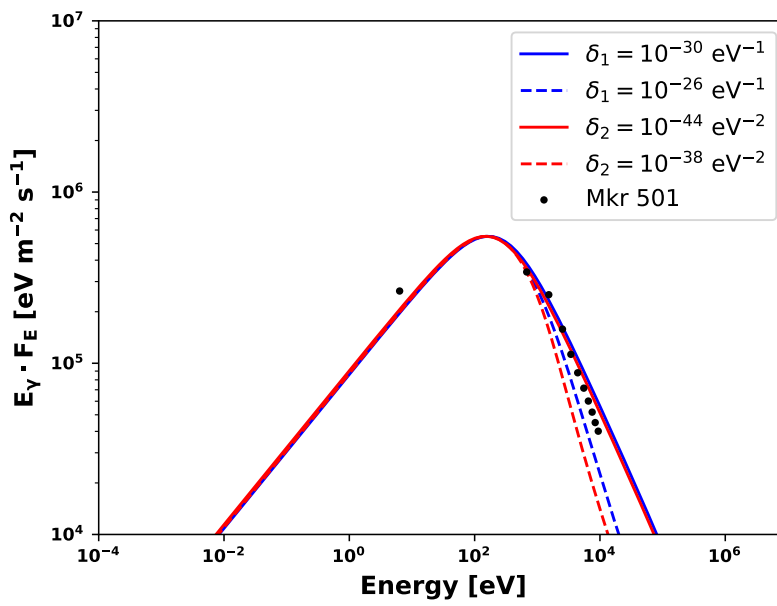


Figure 16. Zoom on the photon's energy spectrum resulting from the synchrotron emission of Markarian 501. The data was taken from [19] and only the synchrotron peak is shown. Different values of $\delta_n^{(e)}$ are shown for both violation orders, $n = 1$ and $n = 2$.

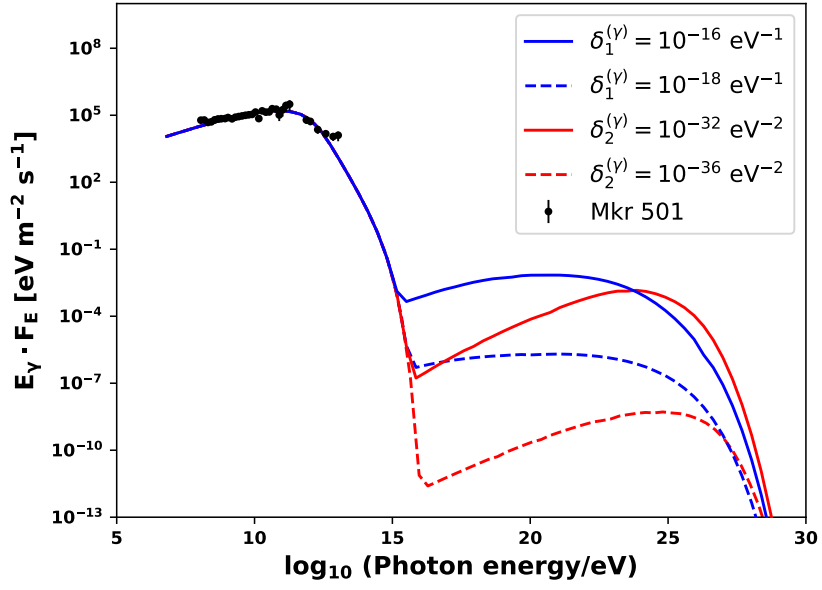


Figure 17. Photon's energy spectrum resulting from the SSC emission of Markarian 501. The data was taken from [19] and only the SSC peak is shown. Different values of $\delta_n^{(\gamma)}$ are shown for both violation orders, $n = 1$ and $n = 2$.

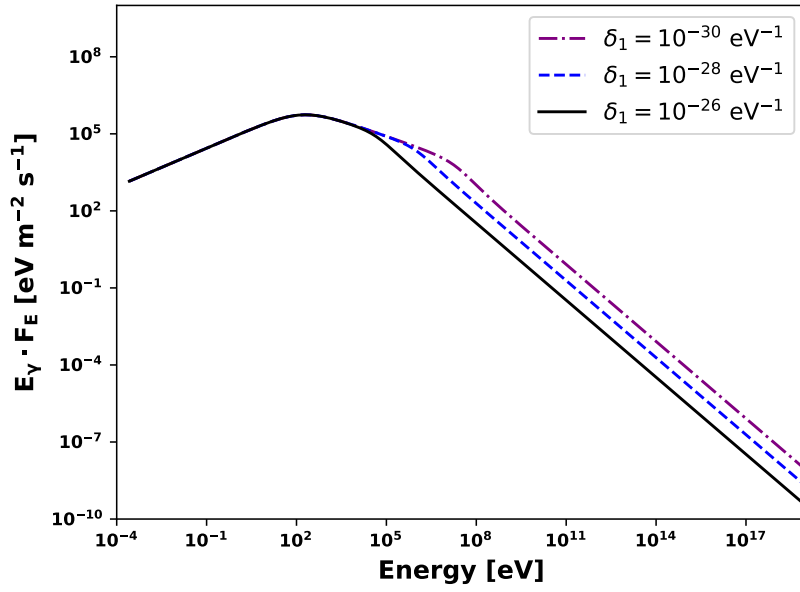


Figure 18. Photon's energy spectrum resulting from the synchrotron emission of a BL Lac object. A cut-off of 10^{14} eV was adopted. The first order of violation, $n = 1$, is shown for different breaking parameters in electrons.

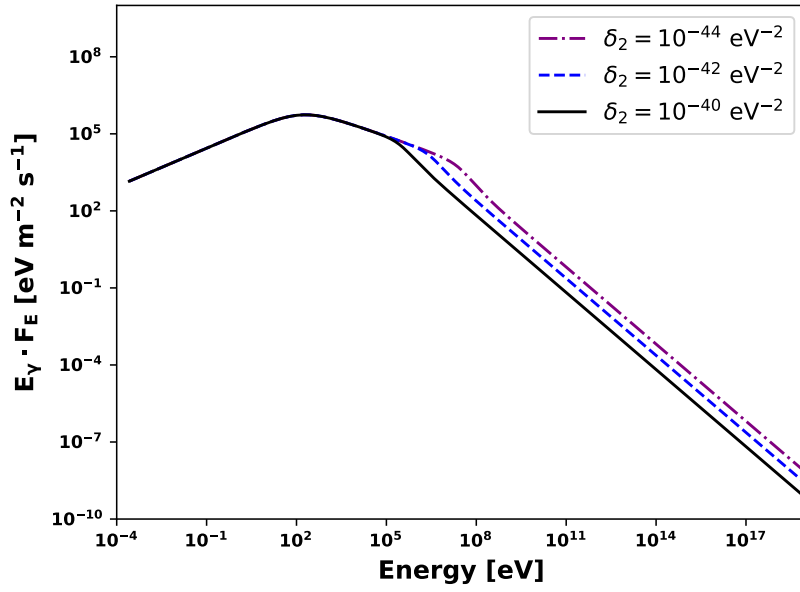


Figure 19. Photon's energy spectrum resulting from the synchrotron emission of a BL Lac object. A cut-off of 10^{14} eV was adopted. The second order of violation, $n = 2$, is shown for different breaking parameters in electrons.

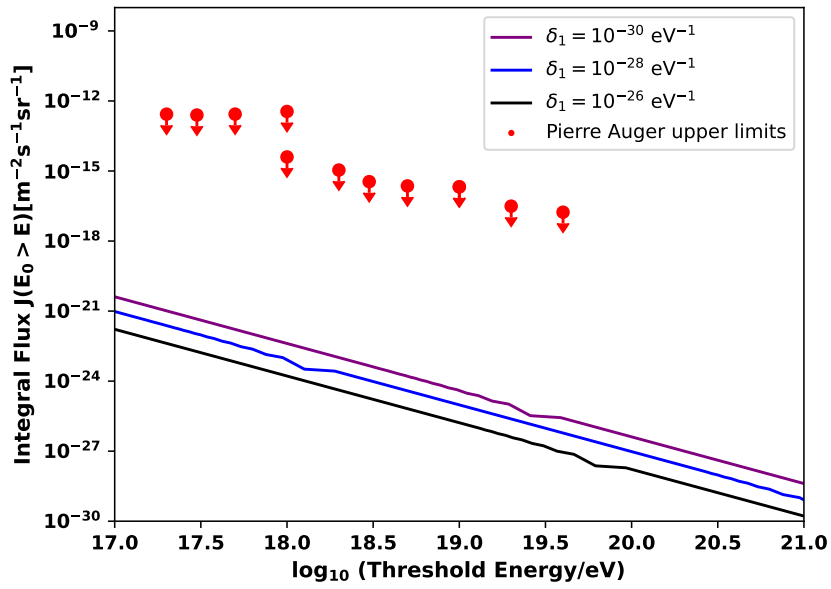


Figure 20. Integral photon flux for energies beyond 10^{17} eV for a violation of order $n = 1$ adopting different values of $\delta_1^{(e)}$. Red dots are the current upper limits set by the Pierre Auger Observatory.

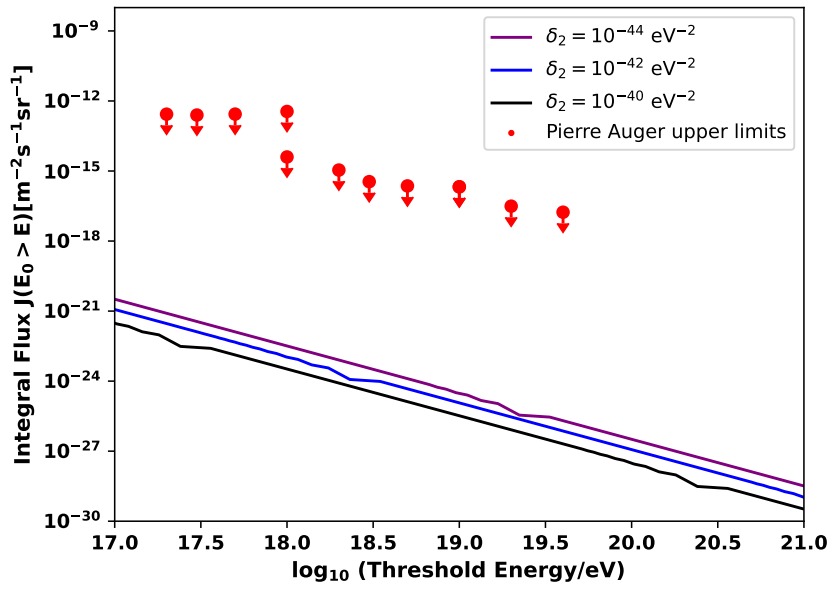


Figure 21. Integral photon flux for energies beyond 10^{17} eV for a violation of order $n = 2$ adopting different values of $\delta_2^{(e)}$. Red dots are the current upper limits set by the Pierre Auger Observatory.

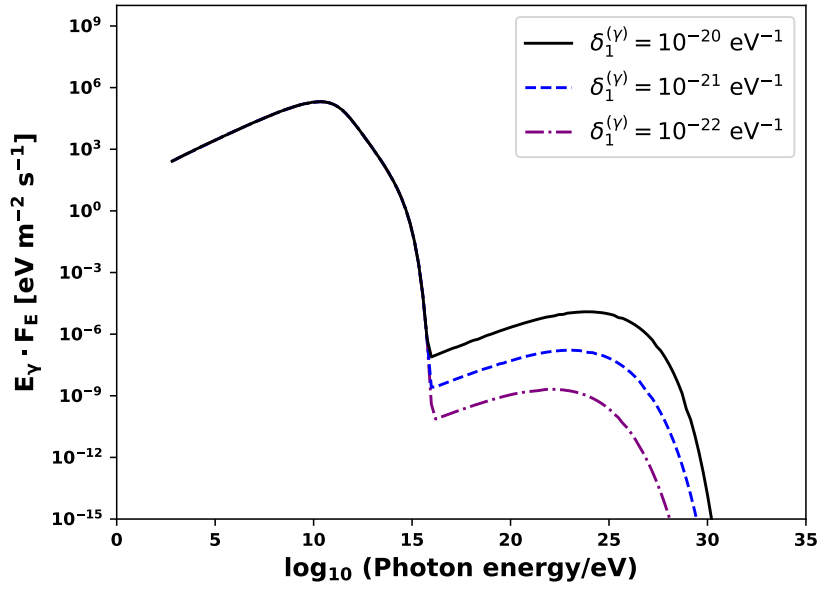


Figure 22. Photon's energy spectrum resulting from the SSC emission of a BL Lac object. A cut-off of 10^{14} eV was adopted. The first order of violation, $n = 1$, is shown for different breaking parameters in photons.

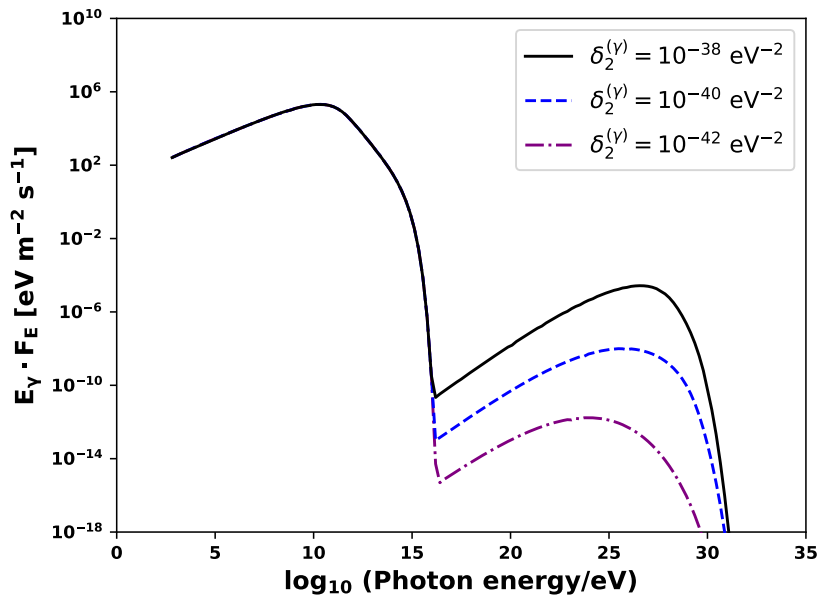


Figure 23. Photon's energy spectrum resulting from the SSC emission of a BL Lac object. A cut-off of 10^{14} eV was adopted. The second order of violation, $n = 2$, is shown for different breaking parameters in photons.

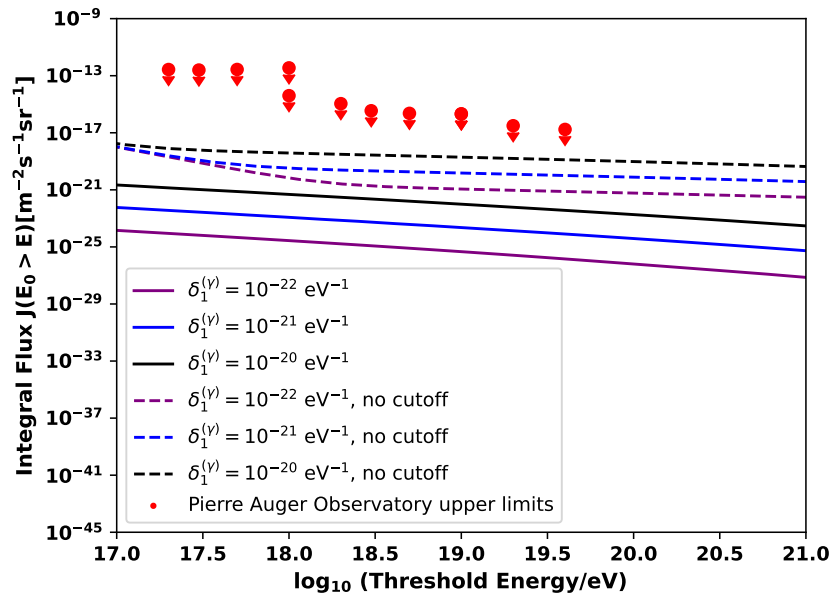


Figure 24. Integral photon flux for energies beyond 10^{17} eV for a violation of order $n = 1$ adopting different values of $\delta_1^{(\gamma)}$. The solid curves are the integral of photon fluxes for a population of 10^3 BL Lac sources with a cut-off of 10^{14} eV. Dashed lines represent the same emission without cut-offs. Red dots are the current upper limits set by the Pierre Auger Observatory.

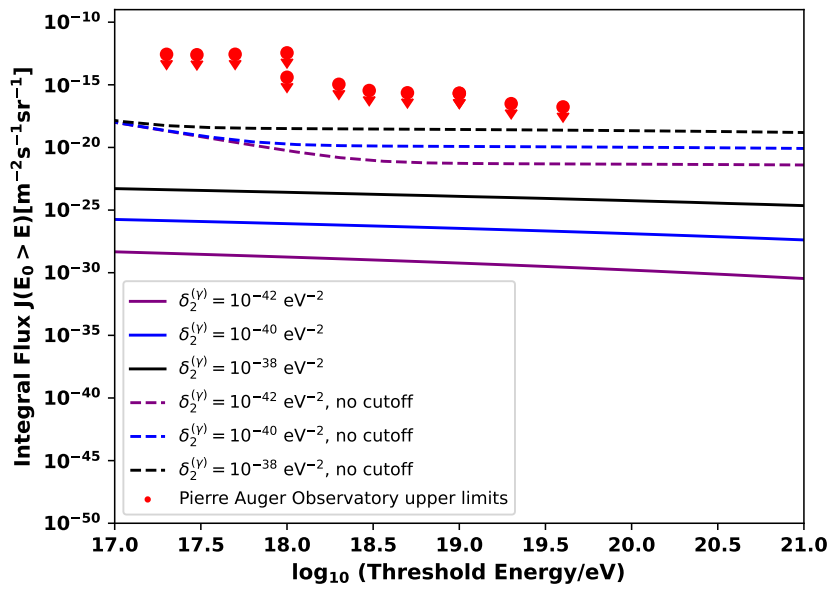


Figure 25. Integral photon flux for energies beyond 10^{17} eV for a violation of order $n = 2$ adopting different values of $\delta_2^{(\gamma)}$. The solid curves are the integral of photon fluxes for a population of 10^3 BL Lac sources with a cut-off of 10^{14} eV. Dashed lines represent the same emission without cut-offs. Red dots are the current upper limits set by the Pierre Auger Observatory.